New Journal of Physics
The open access journal at the forefront of physics

Deutsche Physikalische Gesellschaft DPG
IOP Institute of Physics

Published in partnership with: Deutsche Physikalische Gesellschaft and the Institute of Physics

OPEN ACCESS

RECEIVED
22 May 2017

REVISED
17 August 2017

ACCEPTED FOR PUBLICATION
1 September 2017

PUBLISHED
31 October 2017

PAPER

Vortex formation and dynamics of defects in active nematic shells

Diana Khoromskaia and Gareth P Alexander

Department of Physics and Centre for Complexity Science, University of Warwick, Coventry CV4 7AL, United Kingdom

E-mail: diana.khoromskaia@yahoo.de

Keywords: active nematics, thin film, topological defects, spherical shell, active matter

Abstract

We present a hydrodynamic model for a thin spherical shell of active nematic liquid crystal with an arbitrary configuration of defects. The active flows generated by defects in the director lead to the formation of stable vortices, analogous to those seen in confined systems in flat geometries, which generate effective dynamics for four $+1/2$ defects that reproduces the tetrahedral to planar oscillations observed in experiments. As the activity is increased and two counterrotating vortices dominate the flow, the defects are drawn more tightly into pairs, rotating about antipodal points. We extend this situation to also describe the dynamics of other configurations of defects. For example, two $+1$ defects are found to attract or repel according to the local geometric character of the director field around them and the extensile or contractile nature of the material, while additional pairs of opposite charge defects can give rise to flow states containing more than two vortices. Finally, we describe the generic relationship between defects in the orientation and singular points of the flow, and suggest implications for the three-dimensional nature of the flow and deformation in the shape of the shell.

1. Introduction

Active liquid crystals [1–3] (ALCs) have proved successful as a paradigm for living systems on the microscale, providing insight into processes like cell motility [4–6] and division[7–9], development of cell shapes [10, 11], and growth of cell colonies [12]. Certain fundamental motifs have been developed such as the instability of uniformly aligned states, the emergence of spontaneous flows, the creation and self-propulsion of topological defects and the shear-thinning character of extensile gels. More recently another motif has emerged around confinement of ALCs, where the prominent feature is the emergence of stable flow vortices. For instance, confinement gives rise to a stable single vortex state in dense bacterial suspensions [13, 14], active nematic suspensions [15, 16] and cell monolayers [17, 18]. Circulatory flows are also characteristic of cytoplasmic streaming [6, 16, 19, 20]. As the system size is increased such vortices become unstable [21] and turbulent flows develop, a prevalent feature in bulk active fluids [22–24]. In active systems with high frictional dissipation stable vortices can also arise in the absence of spatial confinement [25–27]. Recent experiments by Keber *et al* on microtubule-based extensile active nematics [28] are realisations of a different type of confined geometry, in which the ALC adheres to the surface of a vesicle. The primary behaviour reported is of four motile $+1/2$ defects in the orientation that undergo regular oscillations between tetrahedral and planar configurations. Here, we develop a hydrodynamic model for a spherical shell of ALC, with arbitrary defect configuration, and find topologically stabilised vortices as a prominent feature of the flow, which reproduces the defect motion from experiments.

Defects in the director are unavoidable on the sphere because of its topology [29]. In the minimal situation there are four, all of strength $+1/2$. Such defects are known to self-propel in ALCs [30], which motivates a minimal description of their motion as a point particle dynamics, and such a model was shown to reproduce the main experimental observations [28]. We extend this to a hydrodynamic model in the confined geometry of a thin spherical shell and show that the dynamics is characterised by the formation of two counterrotating vortices, one in each hemisphere, paralleling the vortex formation seen in other types of confinement [13, 16, 31]. These flows reproduce the tetrahedral to planar oscillations of the four $+1/2$ defects that are found

in experiments and in point-particle models of the dynamics. The oscillations of four half-defects are found to be stable against additional half-defect pairs created randomly in larger shells. If the defects are instead induced at specific positions, it is possible to generate more complex, metastable flow vortex configurations. The oscillations appear above a finite threshold of the activity, below which the defects form static configurations of distorted tetrahedra. Linear stability analysis captures the mode of deformation and the threshold for defect motion. As the activity is increased the two large vortices dominate the flow and the pair of $+1/2$ defects within each are pulled closer together in an effective attraction of like-charge defects. The thin film geometry also leads to new scalings for the defect speed and for the frequency of oscillations.

The dynamics of polar configurations with only integer strength defects is similar and we find hydrodynamic attraction of pairs of aster-like $+1$ defects in extensile active nematic shells, but repulsion for vortex-like defects. The speed of defects in the polar case is shown to have different scaling than for nematic shells, in particular the type of motion does not depend on the radius in the former case whereas it does in the latter.

Just as there are defects in the director field there are also vortices and stagnation points in the flow field, with a total winding of $+2$ according to the Poincaré–Hopf theorem [29]. There is a one-way relationship that assigns to a defect in the director a flow singularity whose winding number depends only on the defect's topological strength. However, in general these flow singularities are not sufficient to satisfy the Poincaré–Hopf theorem and additional vortices also arise in between the director defects. Except in situations of high symmetry their location cannot be simply predicted from the defect positions.

2. Model

We consider an active nematic in a thin spherical shell of thickness h_0 and inner radius R, with $h_0/R = \varepsilon \ll 1$. With tangential alignment of the nematic, as we exclusively consider, there are necessarily defects in the director field, which dominate the elasticity and the active stresses, generating thresholdless active flows [32]. When the elastic relaxation of the director field is rapid compared to the time scale of the active flow dynamics, we can represent the director by a quasi-static equilibrium configuration determined by the positions of the defects. In this regime, the three-dimensional flow $\boldsymbol{u} = (u_r, \boldsymbol{u}_\perp)$ in the shell is driven by gradients in the active stresses and can be found as the solution of the generalised Stokes and continuity equations, $-\nabla p + \mu\Delta\boldsymbol{u} + \nabla\cdot\boldsymbol{\sigma}^a = \boldsymbol{0}$ and $\nabla\cdot\boldsymbol{u} = 0$, where p is the pressure and μ the viscosity. The active stress $\boldsymbol{\sigma}^a = -\sigma_0\left(\boldsymbol{PP} - \frac{1}{3}\mathbb{I}\right)$ is extensile throughout this paper, $\sigma_0 > 0$, in order to relate with microtubule-based active nematics [22, 28], although we comment on the contractile case at the end. If the polarisation $\boldsymbol{P}$ is specified one can solve for the active flow generated by it in a thin film approach [33–37], described in appendix A. We take the polarisation to be tangential throughout the shell thickness, $\boldsymbol{P} = \cos(\psi)\hat{\boldsymbol{e}}_\theta + \sin(\psi)\hat{\boldsymbol{e}}_\phi$, and construct an explicit form for $\psi(\theta, \phi)$ from the positions of the defects. It is convenient to do this using stereographic projection from the complex plane, $z(\theta, \phi) = R\cot(\theta/2)\mathrm{e}^{\mathrm{i}\phi}$. In the plane a nematic director $\boldsymbol{n} = (\cos\alpha, \sin\alpha)$ with n_{def} defects with topological strengths m_j and positions $z_j = x_j + \mathrm{i}y_j$ is given by [38]

$$\alpha = \alpha_0 + \sum_{j=1}^{n_{\mathrm{def}}} \mathrm{Im}\left(\ln(z - z_j)^{m_j}\right), \tag{1}$$

where the phase $\alpha_0 \in [0, \pi)$ parametrises whether the local geometry of the director around a defect is more splay-like or more bend-like. Stereographic projection of this director field onto the sphere yields a polarisation field in the spherical shell via

$$\psi(\theta, \phi) = \phi - \alpha(\theta, \phi). \tag{2}$$

Parametrised in this way, $\boldsymbol{P}$ is an exact minimiser of the elastic energy of a nematic on a sphere in the one-elastic-constant approximation [39]. Moreover, it consists only of those defects from which α is constructed explicitly, provided $\sum_j m_j = 2$.

Applying the thin film approximation (see appendix A) yields the tangential component of the flow, $\boldsymbol{u}_\perp = (u_\theta, u_\phi)$, which in dimensionless variables has the form

$$\tilde{\boldsymbol{u}}_\perp = \tilde{\sigma}_0 f(\tilde{r}) \begin{pmatrix} -\sin(2\psi)\partial_\theta\psi + \frac{\cos(2\psi)}{\sin\theta}(\cos\theta + \partial_\phi\psi) \\ \cos(2\psi)\partial_\theta\psi + \frac{\sin(2\psi)}{\sin\theta}(\cos\theta + \partial_\phi\psi) \end{pmatrix}. \tag{3}$$

The radial profile is $f(\tilde{r}) = \frac{\tilde{r}^2}{2} - \tilde{r}$, where $\tilde{r} \in [0, 1]$ is the radial position within the shell in units of h_0. This solution corresponds to a no-slip inner surface and a vanishing tangential stress on the outer surface, which in principle may deform. Shape changes of the outer surface, given by $h(\theta, \phi)$, are coupled to the radial flow component through the kinematic boundary condition $\partial_t h = u_r(r = h)$ [35]. From incompressibility it follows that $u_r(r = h) = -\boldsymbol{\nabla}_\perp\cdot\bar{\boldsymbol{u}}_\perp$, where $\boldsymbol{\nabla}_\perp \sim 1/R$ is the surface divergence and $\bar{\boldsymbol{u}}_\perp = \int_R^h \boldsymbol{u}_\perp\,\mathrm{d}r \sim h_0 U_0$. So, a small

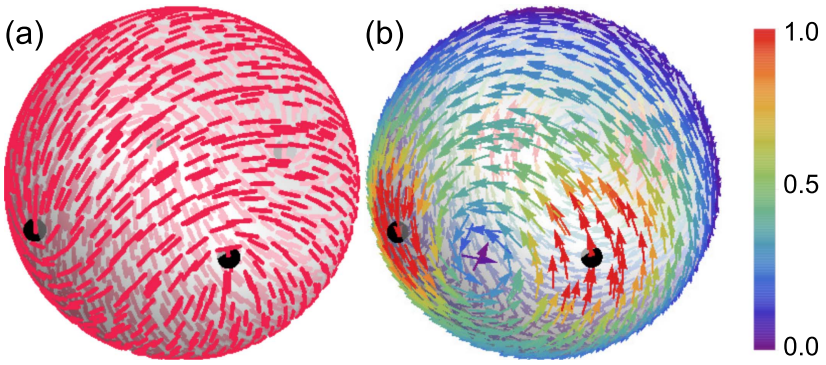

Figure 1. (a) Orientation field $\boldsymbol{P}$ with four $+1/2$ defects in a paired planar configuration. (b) Resulting tangential flow $\tilde{\boldsymbol{u}}_\perp$ from equation (3), showing the typical two-vortex structure. The flow magnitude is colour-coded and cut off in the vicinity of the defects. Here, and in all subsequent figures, only the outer surface of the shell, $\tilde{r} = 1$, is displayed for clarity.

deviation δh away from the spherical shape evolves according to

$$\partial_t(\delta h(t)) = -\boldsymbol{\nabla}_\perp \cdot \tilde{\boldsymbol{u}}_\perp \sim \varepsilon U_0, \tag{4}$$

which is small compared to the tangential flows. We therefore adopt the simplifying assumption that the outer interface remains spherical and does not couple to the defect motion. Locally, changes in the shell thickness may be expected to be similar to the deformations of a thin active drop on a surface, as considered by Joanny and Ramaswamy [36].

Figure 1 gives an example of the director for four $+1/2$ defects in a planar configuration and the corresponding active flow given by equation (3), which is seen to consist of two large counterrotating vortices and two pairs of smaller vortices and stagnation points. This emergence of stable vortices is the germane feature of the active flows on spherical shells.

The director dynamics is dominated by the motion of defects, when the orientational dynamics is rapid [28]. In our approach the director is instantaneously given by the parametrisation (1) as the defect positions change. The defects are advected by the flow they create and we describe their motion in a point-particle description [30, 40, 41]. Each defect moves due to the tangential component of the active flows, given by equation (3), and due to a net force $\boldsymbol{F}_k$ with which all other defects act upon it according to standard nematic elasticity [38]. This force, as given in equation (35)–(37) in appendix B, provides elastic attraction or repulsion of defects depending on their topological strength, with an effective friction coefficient ξ and elastic constant K [28, 42]. The overdamped dynamical system for the defect positions $\boldsymbol{r}_k(t)$ is

$$\frac{\mathrm{d}\boldsymbol{r}_k(t)}{\mathrm{d}t} = \boldsymbol{v}_k(t) + \frac{1}{\xi}\boldsymbol{F}_k(t), \quad k = 1, .., \ n_{\mathrm{def}}. \tag{5}$$

The resultant dynamics is similar to [28], except that here we obtain the advective flow $\boldsymbol{v}_k$ from a self-consistent hydrodynamics in the spherical shell and generalise to an arbitrary collection of defects. Within the thin film approximation the flow diverges in magnitude at the defects, therefore we introduce a short-length cut-off and obtain the velocity of a defect located at (θ_k, ϕ_k) as an average of the flow over a small circle $\gamma_k(s)$ centred at the defect

$$\boldsymbol{v}_k(t) = \frac{1}{2\pi}\oint_{\gamma_k} \boldsymbol{u}_\perp(s, t)\,\mathrm{d}s. \tag{6}$$

For the defect motion the flow is evaluated at the outer surface, where $f(\tilde{r} = 1) = -1/2$. The circle $\gamma_k(s) = (\theta_k + \rho\cos(s), \phi_k + \rho\sin(s)/\sin(\theta_k))$, $s \in [0, 2\pi]$, has the opening angle ρ, which is the dimensionless cut-off length. Since this is where the continuum, thin film description breaks down, it can be associated with either the film thickness or the defect core radius r_c through

$$\rho = \frac{1}{R}\max\{h_0, r_c\}. \tag{7}$$

The core size could be measured for a particular experimental system, for instance as the size of the region around a defect which is devoid of active nematogens, and may depend on other system parameters.

With the time scale of elastic relaxation $\tau = \xi R^2/K$ we define $\tilde{t} = t/\tau$ and equation (5) takes the form

$$\frac{\partial \theta_k}{\partial \tilde{t}} = \frac{\tau}{R} v_{k,\theta} + \frac{\tau}{\xi R} F_{k,\theta}, \tag{8}$$

$$\frac{\partial \phi_k}{\partial \tilde{t}} = \frac{1}{\sin\theta_k}\left(\frac{\tau}{R} v_{k,\phi} + \frac{\tau}{\xi R} F_{k,\phi}\right). \tag{9}$$

This choice of time scale sets the scale of the elastic terms to $\tilde{K} = \tau K/\xi R^2 = 1$. This identifies the scaling of $\tau|\boldsymbol{v}_k|/R$ as the defining parameter for the defect dynamics, which represents the ratio of active to elastic effects and depends on the topological strength of the defect through $|\boldsymbol{v}_k|$. Equations (8) and (9) are integrated numerically for different defect configurations using a standard Runge–Kutta method.

3. Results

3.1. Active flow at the defects

In addition to the singularities in the director, the vortices in figure 1(b) contain singularities in the flow field, about which the flow circulates. Such flow singularities are topologically required [29] and can be generated at the locations of defects in the director. A general relationship between defects and flow singularities follows from evaluating (3) on the small circle $\gamma_k(s)$ and expanding in powers of ρ, the angular distance to the kth defect (see appendix A). We make use of the stereographic projection to write

$$\tilde{u}(\rho) = \tilde{u}_\theta + \mathrm{i}\tilde{u}_\phi = \frac{m_k}{\rho} \mathrm{e}^{\mathrm{i}(2m_k-1)s} \mathrm{e}^{\mathrm{i}2(1-m_k)\phi_k} \mathrm{e}^{-\mathrm{i}2w(z_k)} + \mathcal{O}(1), \tag{10}$$

where $w(z_k) = \alpha_0 + m_k\pi + \sum_{j\neq k} m_j \,\mathrm{Im}\,(\ln(z_k - z_j))$. The dominant contribution to the flow $\tilde{\boldsymbol{u}}_\perp$ near the kth defect diverges as $\sim 1/\rho$ and has the winding number

$$\mathcal{I} = 2m_k - 1. \tag{11}$$

Unit strength defects produce a vortex ($\mathcal{I} = 1$) in the flow. When there are two such defects, at antipodal positions, they generate two counterrotating vortices with no other flow singularities. In fact, this is the only situation in which defect-centred vortices are the only ones present, since only for two unit strength defects the requirement $2 = \sum_k (2m_k - 1)$ is satisfied. On the other hand, simple stagnation points ($\mathcal{I} = -1$) cannot be created at defect locations. For half-integer defects relation (11) was shown in [30, 41] and the flow around a single spiral defect in active polar gels was studied in [43].

In a typical situation the flow singularities at defects are not sufficient to generate a total winding of $+2$. This is most evident for four half-defects, as seen in figure 1(b) where all flow vortices form in between the defects, because for $m_k = 1/2$ the flow is non-winding ($\mathcal{I} = 0$). Instead, it is directed along the defect's symmetry axis,

$$\tilde{u}^{+1/2} = \frac{1}{2\rho} \mathrm{e}^{\mathrm{i}(\phi_k - 2w(z_k))}, \tag{12}$$

which is obtained as the leading order term of equation (10) evaluated for a $+1/2$ defect. For these defects, we approximate the advective flow $\boldsymbol{v}$ in (6) by this well-defined flow direction and the magnitude

$$|\boldsymbol{v}| \sim \frac{U_0}{\rho} = \frac{h_0^2 \sigma_0}{r_c \mu} =: v_0, \tag{13}$$

where $U_0 = h_0^2\sigma_0/R\ \mu$ is the typical active flow magnitude in the thin film approach (see equation (27) in appendix A) and we replaced $\rho = r_c/R$ assuming $r_c > h_0$. Here, the symbol $=:$ indicates that this expression defines the characteristic velocity v_0. If $r_c < h_0$, then the speed becomes $v_0 = h_0\sigma_0/\mu$. In any case, the speed of a $+1/2$ defect does not depend on the shell radius R, because it generates its own advection locally, where the defining length scales are the shell thickness h_0 and, if applicable, the core size r_c. In equations (8) and (9) the scaling of the dimensionless advective term for a $+1/2$ defect is

$$\frac{\tau}{R}|\boldsymbol{v}| \sim \frac{\xi h_0^2 R \sigma_0}{K \mu r_c} =: \nu. \tag{14}$$

The next term in the expansion (10), which is $\mathcal{O}(1)$, is non-winding only for $m_k = 1$ (see equation (32) in appendix A). Therefore, unit strength defects are advected with a flow $\sim U_0$, and the relevant dimensionless parameter becomes

$$\frac{\tau}{R}|\boldsymbol{v}| \sim \frac{\xi h_0^2 \sigma_0}{K\mu} =: \nu^{(1)}. \tag{15}$$

This predicts a different scaling of the defect dynamics in thin polar shells compared to nematic shells. In the former only integer strength defects are present and, notably, the type of motion does not depend on the radius.

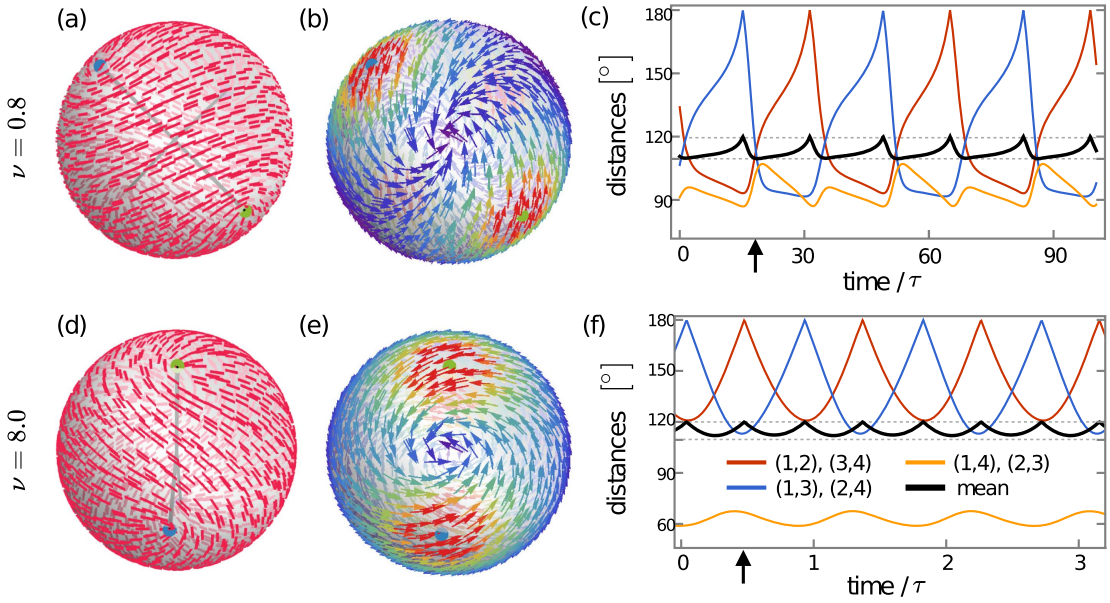

Figure 2. The dynamics of four $+1/2$ defects is characterised by the formation of counterrotating flow vortices and defect pairs. (a)–(c) Tetrahedral-planar oscillations in intermediate activity regime ($\nu = 0.8$); director (a) and flow (b) in tetrahedral configuration at time marked with arrow in (c). (c) Pairwise and mean angular distances between defects; tetrahedral and planar configurations correspond to 109.5° and 120°, respectively. (d)–(f) At higher activity ($\nu = 8.0$) the size of the two main vortices increases and the defect pairs are tighter (see yellow line); director (d) and flow (e) in planar configuration at time marked with arrow in (f); the tetrahedron is no longer approached as seen from pairwise distances in (f). In (c) and (f) (i, j) denotes the distance between defects marked as (i) and (j) in figure 3.

For all other defect types active advection scales at most as $\sim \rho U_0$, which makes it negligible compared to the active motion of $+1/2$ defects. In particular, $-1/2$ defects can be approximated with $\boldsymbol{v} = 0$ in a collection of $\pm 1/2$ defects.

3.2. Four +1/2 defects

In the minimal case of four $+1/2$ defects, the dynamics is determined by the parameter ν, defined in (14). We increase ν through the activity σ_0, keeping all other parameters constant, in particular the radius, in order to fix the time scale τ. The phase α_0 also affects how the defects move. In the ranges $(0,\ \pi/4)$ and $(\pi/4,\ \pi/2)$ the dynamics is similar and we choose $\alpha_0 = \pi/2 - 0.2$ for the examples in the plots. The marginal cases are discussed at the end of this section.

For intermediate activity the positions of the four defects periodically pass through tetrahedral and planar configurations, as shown in figures 2(a)–(c), which is the dynamics found in experiments [28]. The motion is characterised by the formation of two counterrotating flow vortices that separate the defects into two pairs, in which they rotate around each other. This effect becomes more pronounced as the activity is increased, as shown in figures 2(d)–(f). The separation of defects within each pair decreases significantly with ν. There is also a gradual change in the shape of the trajectories, from square-like to more ellipsoid, such that the tetrahedral configurations are no longer approached and the defects oscillate between two different planar arrangements. As the defects in each pair are drawn closer with increasing activity the dynamics approach the situation for two antipodal spirals in the director. In the limit, the flow consists of only one perfectly symmetric flow vortex pair. This behaviour is summarised in figure 3, where the mean and the minimal angular distances are plotted against ν, the latter reflecting the decreasing separation between defects in each pair.

The total speed of the $+1/2$ defects, which also includes motion due to elasticity, is dominated by their active speed v_0 given by (13). The frequency of the defect oscillations is thus

$$f \sim \frac{v_0}{R} = \frac{h_0^2 \sigma_0}{\mu r_c R}, \tag{16}$$

without accounting for the small changes in the orbit shape with increasing ν. As a consequence of the radius-independent defect speed the frequency does depend on the shell size, which provides another route to tuning the defect oscillations.

The effective hydrodynamic attraction of defects into pairs is mediated by the active flow vortices that form in between them, which in turn are controlled by the underlying director. In the tetrahedral configuration the nematic is usually displayed as having a characteristic tennis ball texture [42, 44]. However, for generic values of

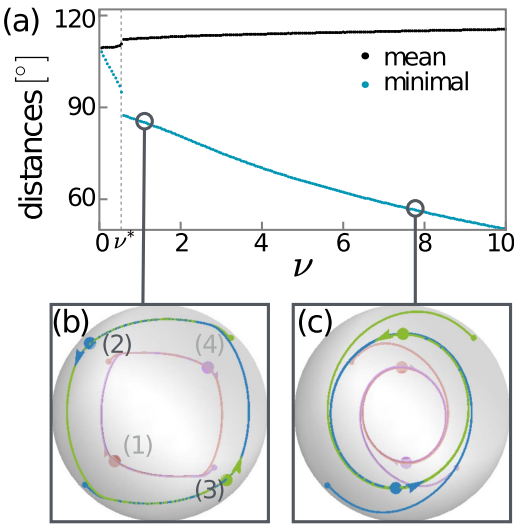

Figure 3. Mean and minimal angular distances between four $+1/2$ defects plotted against ν, the ratio of active to elastic effects. The rapid change in both at $\nu^* \approx 0.7$ marks the transition to the dynamical regime, in which defects move on periodic orbits. The shape of these orbits changes smoothly with ν: (b) square-like trajectories for intermediate activity, corresponding to the tetrahedral-planar oscillations, (c) ellipsoid orbits at higher activity, where defects in each pair have moved closer. In (b) and (c), small dots represent the initial tetrahedral configuration, big dots represent the defect positions at a time corresponding to plots in figure 2 and arrows indicate the direction in which defects traverse the orbits.

α_0 this texture is tilted, see figure 2(a), such that each two half-defects resemble a separated spiral defect. This enables them to approach each other in pairs.

The choices $\alpha_0 = 0,\ \pi/2$ produce no tilt in the texture of the initial tetrahedron and the resulting dynamics lack the contraction of defect trajectories in one of the directions, such that they continue passing through tetrahedra for high activity. Finally, $\alpha_0 = \pi/4$ does not have a dynamical regime and defects relax into increasingly tight, but stationary pairs.

In experiments, active nematic vesicles display a variety of dynamical defect states as well as shape deformations [28]. For intermediate vesicle sizes of about 20 μm the active nematic layer is reported to form four half-integer defects, which move on periodic trajectories similar to those predicted by our model for intermediate values of ν, such as the trajectories in figure 3(b). The time evolution of the mean angular distance in figures 3(c), (f) is also in good agreement with experimentally measured values. It would be interesting to see how this dynamics changes when the vesicle radius is increased. Other structures which are observed instead of four half-defects include an equatorial ring, which occurs in smaller vesicles, and a spindle-like structure that forms from microtubules with higher rigidity. Both are reminiscent of a director with two $+1$ defects, which we consider in section 3.4.

3.3. Linear stability of static configuration

The defects only move above a critical $\nu^* \approx 0.7$ (figure 3) and we describe this transition in a linear stability analysis. The system is initialised with the four defects at the vertices of a tetrahedron with $\theta_i^{(0)} = (\beta,\ \pi - \beta,\ \beta,\ \pi - \beta)$ and $\phi_i^{(0)} = (0,\ \pi/2,\ \pi,\ 3\pi/2)$, with $\beta = \arctan(\sqrt{2})$. It is evident from simulations that for activities below the threshold the defects settle into an increasingly distorted tetrahedron, which can be described by the coordinates

$$\theta_1^* = \theta_3^* = \theta_1^{(0)} - \delta\theta, \tag{17}$$

$$\theta_2^* = \theta_4^* = \theta_2^{(0)} + \delta\theta, \tag{18}$$

$$\phi_1^* = \phi_1^{(0)} - \delta\phi,\ \ \phi_2^* = \phi_2^{(0)} + \delta\phi, \tag{19}$$

$$\phi_3^* = \phi_3^{(0)} - \delta\phi,\ \ \phi_4^* = \phi_4^{(0)} + \delta\phi, \tag{20}$$

with small deviations $\delta\theta$ and $\delta\phi$ as shown in figure 4(a). Using this ansatz we find analytical solutions for the two deviations at linear order. The deformation of the tetrahedron is a superposition of two modes—twisting around and stretching along the z-axis, illustrated in the inset of figure 4(a).

In order to study the linear stability of the skewed tetrahedron that the four defects settle into for low activity we write their dynamical equations as

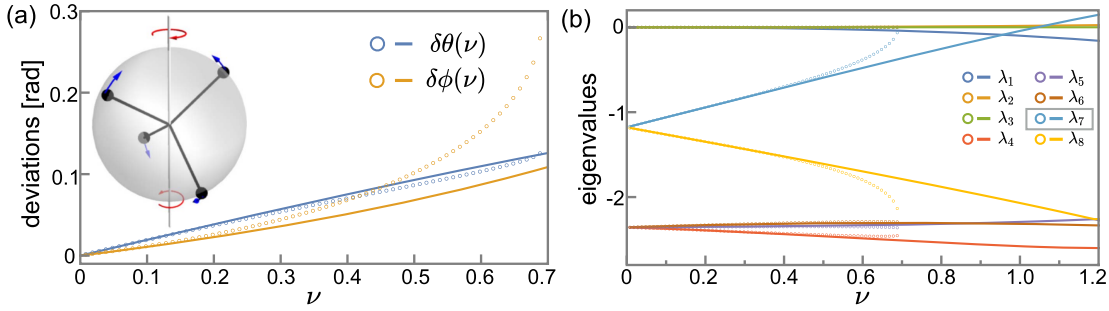

Figure 4. (a) Deviations of defect positions from the tetrahedron in the small activity regime. Shown are deviations $\delta\theta$ and $\delta\phi$ measured in simulations (circles) and obtained from an analytical solution for the stationary configuration at linear order (lines). *Inset:* the corresponding twist (red arrows) and stretching (blue arrows) modes of deformation of the initial tetrahedron. (b) Spectrum of $\boldsymbol{\nabla g}$ evaluated at the 'skewed tetrahedron', using defect positions from the simulation (circles) and positions obtained from analytical expressions for $\delta\theta(\nu)$ and $\delta\phi(\nu)$ given in (22) and (23) (lines). The data suggests that at $\nu^* = 0.7$ the eigenvalue λ_7 (boxed) becomes positive, which renders the 'skewed tetrahedron' linearly unstable. This is qualitatively confirmed by the theoretical prediction, albeit with an overestimated critical activity.

$$\frac{\mathrm{d}\boldsymbol{x}(t)}{\mathrm{d}t} = \boldsymbol{g}(\boldsymbol{x}(t)), \tag{21}$$

where $\boldsymbol{x}(t) = (\theta_1(t), \ldots, \theta_4(t), \phi_1(t), \ldots, \phi_4(t)) \in \mathbb{R}^8$ is the vector of spherical defect coordinates and $\boldsymbol{g}(\boldsymbol{x}(t))$ are the concatenated right-hand sides of equations (38) and (39) in appendix B. We use the ansatz given by (17)–(20) for the fixed point $\boldsymbol{x}^*$ representing the skewed tetrahedron, with $0 < \delta\theta,\ \delta\phi \ll 1$. Linearised in $\delta\theta$ and $\delta\phi$, the stationary condition $\boldsymbol{g}(\boldsymbol{x}(\delta\theta,\ \delta\phi)) = \boldsymbol{0}$ has the solutions

$$\delta\theta(\nu,\ \alpha_0) = -\frac{2\nu(\pi\cos(2\alpha_0) + \sqrt{2}\,\nu)}{2\nu^2\sin^2(2\alpha_0) + 3\pi\sqrt{2}\,\nu\cos(2\alpha_0) + 3\pi^2}, \tag{22}$$

$$\delta\phi(\nu,\ \alpha_0) = \frac{2\sqrt{3}\,\nu(3\sqrt{2}\,\pi - 2\nu\cos(2\alpha_0))}{12\nu^2\sin(2\alpha_0) + 9\pi\,\csc(\alpha_0)\sec(\alpha_0)(\sqrt{2}\,\nu\cos(2\alpha_0) + \pi)}, \tag{23}$$

which are plotted in figure 4(a) together with the deviations measured in the simulations.

At a critical activity the skewed tetrahedron becomes linearly unstable. A perturbation $\delta\boldsymbol{x}$ away from $\boldsymbol{x}^* = (\theta_1^*, \ldots, \phi_4^*)$ evolves according to

$$\frac{\mathrm{d}\delta\boldsymbol{x}}{\mathrm{d}t} = \boldsymbol{\nabla g}|_{\boldsymbol{x}^*} \cdot \delta\boldsymbol{x}, \tag{24}$$

and the spectrum of the dynamical matrix $\boldsymbol{\nabla g}|_{\boldsymbol{x}^*}$ characterises the linear stability of $\boldsymbol{x}^*$. The spectrum is plotted in figure 4(b), calculated numerically from measured deviations and from the approximate solutions (22) and (23), respectively. The simulation data suggests that one eigenvalue changes sign at ν^*, while all others stay non-positive, indicating that the skewed tetrahedron is stable below ν^*. The three vanishing eigenvalues correspond to rigid body rotations. Calculating the eigensystem using the analytical solutions for the deviations above the threshold allows to identify the mode that becomes unstable, albeit with an overestimated critical activity. The eigenvalue λ_7 becomes positive at $\nu \approx 1.0$, which marks the linear instability of the skewed tetrahedron towards a deformation that strongly increases the twist and slightly reverses the stretching. This can be seen from the corresponding eigenvector, which is of the form $(a, -a, a, -a, -b, b, -b, b)$ with $b \gg a > 0$, and this is exactly the dynamics found in simulations at the beginning of the periodic orbits (see figures 3(b) and (c)).

3.4. Two +1 defects

ALCs can develop unit strength defects in their orientation [43, 45] and the confinement to a spherical shell provides a setup where two such defects could be topologically stabilised. We study the advection of two +1 defects in the limit of very strong activity, setting $\tilde{K} = 0$ and using the active time scale $T = R^2\,\mu/h_0^2\sigma_0$. The value of α_0 that is required to generate a particular director geometry at the defects depends on their position. This ambiguity can be removed by setting $\alpha_0 = -\arg(z_1 - z_2) + \tilde{\alpha}_0$, where the additional constant is found by imposing an aster-geometry for $\tilde{\alpha}_0 = 0$ for both defects irrespective of their position. Now, $\tilde{\alpha}_0 \in [0,\ \pi/2]$ produces increasingly tilted spirals, up to two pure vortex defects for $\tilde{\alpha}_0 = \pi/2$.

When the two +1 defects are antipodal there is no advection and the flow again consists of two counterrotating vortices, which coincides with four half-defects in the limit of high activity. If the angular distance of the two +1 defects is $<\pi$, we find that they are either attracted to or repelled from each other by active advection, depending on the local director geometry, as shown in figure 5(a). Two defects that are aster-like ($0 \leqslant \tilde{\alpha}_0 < \pi/4$) experience active hydrodynamic repulsion and relax into an antipodal configuration. Vortex-

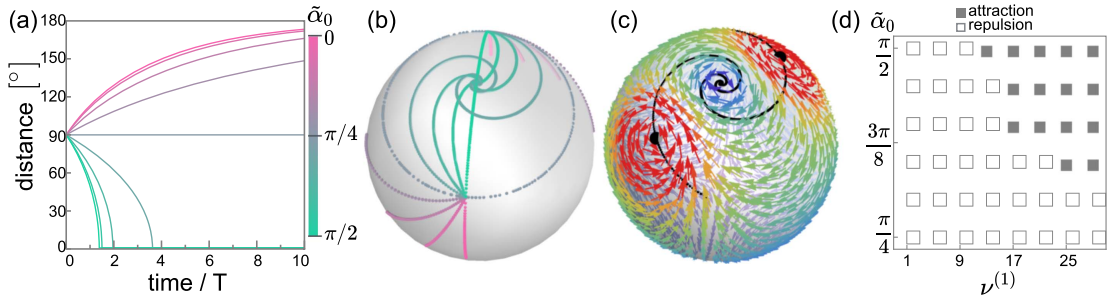

Figure 5. Active advection leads to repulsion of two aster-like defects and attraction of two vortex-like defects on a sphere. (a) Distance of the two +1 defects over time for different local director geometry, controlled by $\tilde{\alpha}_0$, which varies in steps of $\pi/16$. Here, the motion of defects is due to active advection only, with $\tilde{K} = 0$. (b) Perfect asters ($\tilde{\alpha}_0 = 0$) or vortex defects ($\tilde{\alpha}_0 = \pi/2$) move along geodesics, but in general the defects move on outward or inward spiralling trajectories. Two perfect spirals ($\tilde{\alpha}_0 = \pi/4$) move along a circular path, without changing their distance. (c) Two spiral-like defects ($\tilde{\alpha}_0 = 5\pi/16$) are attracted to each other by the flow vortex that forms in between them; their inward spiralling trajectories are shown in black. (d) When elasticity is included, attraction of +1 defects is found only for $\nu^{(1)}$ above a threshold and for large enough tilt $\tilde{\alpha}_0$.

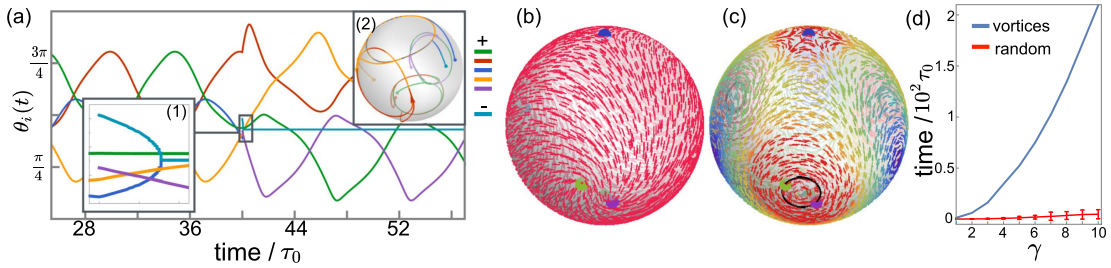

Figure 6. (a) Four $+1/2$ defects show regular oscillations before and shortly after the insertion of an additional $\pm 1/2$ defect pair, as seen from $\theta_i(t)$ for $i = 1, \ldots, 6$ with $\gamma = 2$. *Inset 1:* close-up on the rapid annihilation of the additional pair. *Inset 2:* defects resume similar trajectories after the fluctuation, but with different pairing. (b) Orientation field with eight defects, six $+1/2$ and two $-1/2$, producing a metastable flow vortex arrangement. (c) Corresponding flow structure with six equidistant vortices on the equator, $+1/2$ defect trajectories marked in black. (d) Time to first annihilation event over γ, which is related to the shell radius through $R = \gamma R_0$, for the vortex configuration in (b), (c) and averaged over 500 random initial defect positions.

like defects ($\pi/4 < \tilde{\alpha}_0 \leqslant \pi/2$) show the converse effect and are drawn towards each other. In this idealised setting without elasticity, they would merge into a +2 boojum, with a local flow structure of a +3 singularity accompanied by a stagnation point at the antipodal point. Two perfect spiral defects ($\tilde{\alpha}_0 = \pi/4$) keep a constant distance, rotating around each other on a circular path.

During this motion the defects are typically spiralling inward or outward, as shown in figure 5(b). Only in the two limiting cases do the defects move along their connecting geodesic. Figure 5(c) shows the active flow with the additional vortex in between the defects ($\tilde{\alpha}_0 = 5\pi/16$), that draws the defects inward on a spiralling trajectory. The defects' trajectory rotates in a direction opposite to the rotation of their local flow vortices.

When elastic repulsion is included, with $\tilde{K} = 1$, the defects relax into the antipodal configuration for all $\tilde{\alpha}_0$ for activities up to $\nu^{(1)} \approx 12$. Above this threshold active attraction overbalances the elastic repulsion for large enough $\tilde{\alpha}_0$, as shown in figure 5(d). Interestingly, in such cases the defects again collapse into a very tight pair rather than equilibrating at some finite distance. In an experimental system, fluctuations in the tilt of a spiral around the limiting value of $\tilde{\alpha}_0$ might therefore lead to oscillations between the antipodal and the collapsed configurations.

3.5. Many-defect states

When the activity $|\sigma_0|$ or the shell size R are increased additional $\pm 1/2$ defect pairs may be created on top of the four $+1/2$ defects, as the system approaches the onset of active turbulence [24]. To study such situations we increase the radius as $R = \gamma R_0$, with $\gamma > 1$, keeping all other parameters fixed. This changes the elastic time scale to $\tau = \gamma^2 \tau_0$ and the activity-to-elasticity ratio to $\nu = \gamma \nu_0$. The reference values correspond to parameters in section 3. A for the regime of tetrahedral-planar oscillations with $\nu_0 = 1$.

We consider a system with four defects in this oscillatory state and inject one $\pm 1/2$ pair at a random position. Figure 6(a) shows how the dynamics react to this perturbation. One of the $+1/2$ defects very quickly annihilates with the $-1/2$ and the remaining four defects resume the oscillation, usually in a different pairing. Similarly, when all defects are placed at random positions the annihilation events happen rapidly, leaving the

minimal four-defect state in the oscillating regime. The same is found for more than one additional pair of half-defects in the system. This indicates that the oscillatory state is stable, as long as additional defect pairs occur as fluctuations and are not produced continually. In the simulation, defect annihilation is realised by removing the $\pm 1/2$ defect pair from the director (1) if their distance falls below a pre-defined threshold.

On the other hand, by inducing additional $\pm 1/2$ defects at specific locations more complex flow vortex configurations may be constructed, in which elastic forces and active flows are balanced. The simplest many-defect configuration that is metastable has $n_{\mathrm{pair}} = 2$ additional defect pairs, shown in figures 6(b), (c). The six $+1/2$ defects are allocated to three flow vortices arranged equidistantly around the equator, with another three vortices rotating in the opposite direction in between them. The three-fold symmetry of this flow field is guided by the flow singularities at the $-1/2$ defects, which have $\mathcal{I} = -2$ and are located at the poles. This configuration is transient and reduces to the four-defect state due to coalescence of oppositely charged defects. In figure 6(d) the times to the first annihilation event for this metastable configuration and for $n_{\mathrm{pair}} = 2$ with random initial defect positions are compared. For the vortex configuration this time increases considerably with γ. This opens an interesting direction of tuning specific many-defect states before the onset of active turbulence by exploiting the topologically required singularities in both flow and director. The metastability of such configurations could be aided by an advantageous manipulation of the shell shape, for instance by trapping positive defects in regions of higher curvature [46].

4. Discussion

Our results can be extended to contractile active fluids by changing the sign of the activity σ_0. The reversed sign of the flow exchanges the role of splay-like and bend-like distortions in the orientation. The direction of motion of half-integer defects is reversed, but the tetrahedral-planar oscillations and the formation of vortices—with opposite rotation sense—is unchanged. Similarly, the type of active interaction between $+1$ defects is reversed. The thin film approach used here allows for a non-zero radial flow component, which in general is present in the examples considered and enables the repulsion or attraction of defects due to active flows. The radial component is small, $\sim\mathcal{O}(h_0/R)$, compared to tangential flows and will result in a dynamic deviation from the spherical shape that complements the defect motion. Stationary shell shapes, e.g. for two asters, should locally resemble profiles found for flat droplets of active nematics with defects [36, 37]. We have taken a one elastic constant approximation and isotropic viscosity for simplicity, but in systems of elongated filaments one can expect anisotropy. In particular, long flexible nematogens are much more compliant to bend distortions than to splay [47]. If anisotropy is sufficiently large it could lead to qualitative changes of the dynamics, which is certainly an extension worth pursuing.

Our approach provides a closed form solution for the active fluid flow in an active nematic shell within the thin film approximation, thus allowing to study the advection of defects with arbitrary topological strengths in an efficient, particle-like dynamics. The simplified representation of the director and its time evolution enables us to make theoretical predictions for certain aspects of this dynamics, such as defect velocities, the onset of the dynamical regime, and dependence on shell radius. However, to explore the full range of possible dynamics of active nematic shells numerical solutions of nemato-hydrodynamic equations might be better suited, such as the recent numerical study of half-defect dynamics for a wider range of activities including the transition to an active turbulent regime [48]. Other interesting directions, which would be relevant for a comparison with experiments, include deviations from the spherical shape and variation of elastic constants.

Our work establishes the formation of vortices under confinement as a generic feature also for ALCs on spherical surfaces. It would be interesting to extend to other topologies, for instance tori with additional handles [49].

Acknowledgments

We thank Carl Whitfield, Daniel Pearce and Julia Yeomans for enlightening discussions on various aspects of this work. This work was supported by the UK EPSRC through Grant No. A.MACX.0002.

Appendix A. Flow in a thin active nematic shell

In a thin spherical film of active nematics the generalised Stokes equation given in the main text can be expanded in the small parameter $\varepsilon = h_0/R$. Using the typical magnitude $U_0 = R/T$ of active flows, with an active time scale T, the dimensionless velocity components are $\tilde{u}_\theta = u_\theta/U_0$, $\tilde{u}_\phi = u_\phi/U_0$, and $\tilde{u}_r = u_r/\varepsilon U_0$. The radial coordinate becomes

$$\tilde{r} = \frac{1}{\varepsilon}\left(\frac{r}{R} - 1\right),$$

and the corresponding partial derivatives $\partial_r f = \frac{1}{h_0}\partial_{\tilde{r}} f$, for some function $f(r)$. In the dimensionless form, for instance the θ-component of the Stokes equation becomes

$$0 = -\frac{\varepsilon^2 R}{\mu U_0}\partial_\theta p + \frac{\varepsilon^2 R^2}{\mu U_0}(\nabla \cdot \boldsymbol{\sigma}^a)_\theta + \partial_{\tilde{r}}^2 \tilde{u}_\theta + \mathcal{O}(\varepsilon^2), \tag{25}$$

and there is a similar expression for the ϕ-component. The divergence of the active stress is

$$\nabla \cdot \boldsymbol{\sigma}^a = -\frac{\sigma_0}{R}\begin{pmatrix} 1 \\ -\sin(2\psi)\partial_\theta\psi + \frac{\cos(2\psi)}{\sin\theta}(\cos\theta + \partial_\phi\psi) \\ \cos(2\psi)\partial_\theta\psi + \frac{\sin(2\psi)}{\sin\theta}(\cos\theta + \partial_\phi\psi) \end{pmatrix}. \tag{26}$$

Therefore, in order for the activity to drive the tangential flows the corresponding prefactor in (25) has to scale as $\mathcal{O}(1)$, leading to the dimensionless prefactor

$$\tilde{\sigma}_0 = \frac{\varepsilon^2 R}{\mu U_0}\sigma_0 \tag{27}$$

and a similar relation for the pressure. Analogous to planar thin films [33, 36, 37], the leading order part of the r-component of the Stokes equation yields a constant pressure. With the boundary conditions

$$\partial_{\tilde{r}_s}\tilde{u}_\phi|_{\tilde{r}_s=1} = 0 \quad \text{and} \quad \tilde{u}_\phi|_{\tilde{r}_s=0} = 0, \tag{28}$$

the solution (3) for the tangential flow components is obtained.

For a fixed $\tilde{r}$, for instance $\tilde{r} = 1$ used for the defect dynamics, the tangential flow can be written in a complex representation making use of the stereographic projection $z(\theta, \phi) = R\cot(\theta/2)e^{i\phi}$. In this way, the projection point is the north pole and the plane crosses the sphere along the equator. The complex flow is given by

$$\tilde{u}(z, \bar{z}) = \tilde{u}_\theta + i\tilde{u}_\phi = -\frac{\tilde{\sigma}_0}{2}e^{-i2\alpha(z,\bar{z})}\left\{\frac{z^2}{R|z|} - \frac{z}{2}\left(\frac{R}{|z|} + \frac{|z|}{R}\right)\sum_{j=1}^{n_{\text{def}}} m_j \frac{z - z_j}{|z - z_j|^2}\right\}. \tag{29}$$

This expression is well-defined through the stereographic projection of the tangential flow onto the plane, which is given in the complex form as $u = u_x + iu_y$ and relates to $\tilde{u}$ as

$$\tilde{u} = -(1 - \cos\theta)e^{i\phi}\bar{u}, \tag{30}$$

where $\bar{u}$ denotes the complex conjugate of u. We evaluate (29) on the projection of the small circle $\gamma_k(s)$ introduced in the main text, which has the form

$$z(s) = z_k - \frac{\rho R}{1 - \cos\theta_k}e^{i(\phi_k - s)} \tag{31}$$

with $s \in [0, 2\pi]$, provided the circle does not enclose one of the poles on the sphere. An expansion of (29) in powers of ρ reads

$$\begin{aligned}\tilde{u}(\rho) = {} & \frac{m_k}{\rho}e^{i(2m_k-1)s}e^{i2(1-m_k)\phi_k}e^{-i2w(z_k)} \\ & + e^{-i2w(z_k)}e^{-i2m_k\phi_k}\left\{\frac{m_k}{2}e^{i2(m_k-1)s}e^{i2\phi_k}h_1(z_1, \bar{z}_1, \ldots) + e^{i2m_k s}h_2(z_1, \bar{z}_1, \ldots)\right\} + \mathcal{O}(\rho),\end{aligned} \tag{32}$$

where the functions h_1 and h_2 only depend on the defect positions and other constants. Integrating this expression over s yields a non-winding contribution at the order $\mathcal{O}(1/\rho)$ for $m_k = 1/2$ and at the order $\mathcal{O}(1)$ for $m_k = 1$, as discussed in the main text.

Appendix B. Point-particle-like dynamics of defects

The free energy of a nematic on a sphere can be phrased in terms of the defects' pairwise interaction energies and their self-energies [39, 42, 44], which are constant in our model,

$$E = -\frac{\pi K}{2}\sum_{\substack{i,j=1 \\ i\neq j}}^{n_{\text{def}}} m_i m_j \ln(1 - \cos\beta_{ij}) + \text{const.} \tag{33}$$

The angular distance between defect i and j is given by

$$\cos\beta_{ij} = \cos\theta_i\cos\theta_j + \sin\theta_i\sin\theta_j\cos(\phi_i - \phi_j). \tag{34}$$

The force acting on defect k due to all other defects is [28, 38]

$$\boldsymbol{F}^{(k)} = -\boldsymbol{\nabla}_k E = -\left(\hat{\boldsymbol{e}}_{\theta,k}\frac{1}{R}\partial_{\theta_k}E + \hat{\boldsymbol{e}}_{\phi,k}\frac{1}{R\sin\theta_k}\partial_{\phi_k}E\right), \tag{35}$$

where the notations $\hat{\boldsymbol{e}}_{\theta,k} = \cos\theta_k(\cos\phi_k\hat{\boldsymbol{e}}_x + \sin\phi_k\hat{\boldsymbol{e}}_y) - \sin\theta_k\hat{\boldsymbol{e}}_z$ and $\hat{\boldsymbol{e}}_{\phi,k} = -\sin\phi_k\hat{\boldsymbol{e}}_x + \cos\phi_k\hat{\boldsymbol{e}}_y$ are used. The θ-component of (35) contains

$$\partial_{\theta_k}E = K\pi m_k\sum_{j=1,j\neq k}^{n_{\rm def}} m_j\frac{\partial_{\theta_k}\cos\beta_{kj}}{1-\cos\beta_{kj}} \tag{36}$$

and the expression for $\partial_{\phi_k}E$ is analogous. The elastic terms in the dimensionless dynamical equations (8) and (9) can be written as

$$\frac{\tau}{\xi R}F_\theta^{(k)} = -\frac{\tau K}{\xi R^2}\pi m_k\sum_{j=1,j\neq k}^{n_{\rm def}} m_j\frac{\partial_{\theta_k}\cos\beta_{kj}}{1-\cos\beta_{kj}}, \tag{37}$$

and a similar expression for the ϕ-component. Making time dimensionless with τ leads to $\tilde{K} = \tau K/\xi R^2 = 1$.

For example, for four $+1/2$ defects the full dynamical system reads

$$\partial_{\tilde{t}}\theta_k = -\frac{\pi}{4}\sum_{j=1,j\neq k}^{4}\frac{\partial_{\theta_k}\cos\beta_{kj}}{1-\cos\beta_{kj}} - \frac{\nu}{4}\cos(\phi_k - 2w(z_k)), \tag{38}$$

$$\partial_{\tilde{t}}\phi_k = \frac{1}{\sin\theta_k}\left(-\frac{\pi}{4\sin\theta_k}\sum_{j=1,j\neq k}^{4}\frac{\partial_{\phi_k}\cos\beta_{kj}}{1-\cos\beta_{kj}} - \frac{\nu}{4}\sin(\phi_k - 2w(z_k))\right) \tag{39}$$

for $k = 1,\ldots,4$, where $w(z_k) = \alpha_0 + \frac{\pi}{2} + \frac{1}{2}\sum_{j\neq k}\mathrm{Im}\{\ln(z_k - z_j)\}$ and ν is defined in equation (14) in the main text.

For all defect configurations the dynamical systems are integrated using the ordinary differential equation solver `ode23s` provided by the software *MATLAB 2016a*, with relative and absolute accuracies set to $10^{-6}\tau$.

ORCID iDs

Diana Khoromskaia https://orcid.org/0000-0003-2597-6336

References

[1] Prost J, Jülicher F and Joanny J F 2015 *Nat. Phys.* **11** 111
[2] Marchetti M C, Joanny J F, Ramaswamy S, Liverpool T B, Prost J, Rao M and Simha R A 2013 *Rev. Mod. Phys.* **85** 1143
[3] Ramaswamy S 2010 *Annu. Rev. Condens. Matter Phys.* **1** 323
[4] Kruse K, Joanny J F, Jülicher F and Prost J 2006 *Phys. Biol.* **3** 130
[5] Tjhung E, Tiribocchi A, Marenduzzo D and Cates M E 2015 *Nat. Commun.* **6** 5420
[6] Tjhung E, Marenduzzo D and Cates M E 2012 *Proc. Natl Acad. Sci. USA* **109** 12381
[7] Salbreux G, Prost J and Joanny J F 2009 *Phys. Rev. Lett.* **103** 058102
[8] Turlier H, Audoly B, Prost J and Joanny J F 2014 *Biophys. J.* **106** 114
[9] Brugués J and Needleman D 2014 *Proc. Natl Acad. Sci. USA* **111** 18496
[10] Salbreux G, Joanny J F, Prost J and Pullarkat P 2007 *Phys. Biol.* **4** 268
[11] Callan-Jones A C, Ruprecht V, Wieser S, Heisenberg C P and Voituriez R 2016 *Phys. Rev. Lett.* **116** 028102
[12] Doostmohammadi A, Thampi S P and Yeomans J M 2016 *Phys. Rev. Lett.* **117** 048102
[13] Wioland H, Woodhouse F G, Dunkel J, Kessler J O and Goldstein R E 2013 *Phys. Rev. Lett.* **110** 268102
[14] Wioland H, Woodhouse F G, Dunkel J and Goldstein R E 2016 *Nat. Phys.* **12** 341
[15] Guillamat P, Ignés-Mullol J and Sagués F 2017 Control of active nematics with passive liquid crystals *Mol. Cryst. Liq. Cryst.* **646** 226–34
[16] Woodhouse F G and Goldstein R E 2012 *Phys. Rev. Lett.* **109** 168105
[17] Segerer F J, Thüroff F, Piera Alberola A, Frey E and Rädler J O 2015 *Phys. Rev. Lett.* **114** 228102
[18] Mohammad Nejad T, Iannaccone S, Rutherford W, Iannaccone P M and Foster C D 2014 *Biomech. Model. Mechanobiol.* **14** 107
[19] Whitfield C A, Marenduzzo D, Voituriez R and Hawkins R J 2014 *Eur. Phys. J.* E **37** 8
[20] Kumar A, Maitra A, Sumit M, Ramaswamy S and Shivashankar G V 2014 *Sci. Rep.* **4** 3781
[21] Simha A R and Ramaswamy S 2002 *Phys. Rev. Lett.* **89** 058101
[22] Sanchez T, Chen D T N, DeCamp S J, Heymann M and Dogic Z 2013 *Nature* **491** 431–4
[23] Dunkel J, Heidenreich S, Drescher K, Wensink H H, Bär M and Goldstein R E 2013 *Phys. Rev. Lett.* **110** 228102
[24] Giomi L 2015 *Phys. Rev.* X **5** 031003
[25] Adamer M F, Thampi S P, Yeomans J M and Doostmohammadi A 2016 *Nat. Commun.* **7** 10557
[26] Schaller V, Weber C, Semmrich C, Frey E and Bausch A R 2010 *Nature* **467** 73
[27] Sumino Y, Nagai K H, Shitaka Y, Tanaka D, Yoshikawa K, Chaté H and Oiwa K 2012 *Nature* **483** 448
[28] Keber F C, Loiseau E, Sanchez T, DeCamp S J, Giomi L, Bowick M J, Marchetti M C, Dogic Z and Bausch A R 2014 *Science* **345** 1135

[29] Hopf H 1989 *Differential Geometry in the Large* (Berlin: Springer)
[30] Giomi L, Bowick M J, Mishra P, Sknepnek R and Marchetti C M 2014 *Phil. Trans. R. Soc.* A **372** 20130365
[31] Sknepnek R and Henkes S 2015 *Phys. Rev.* E **91** 022306
[32] Green R, Toner J and Vitelli V 2016 (arXiv:1602.00561)
[33] Oron A, Davis S H and Bankoff S G 1997 *Rev. Mod. Phys.* **69** 931
[34] Takagi D and Huppert H E 2010 *J. Fluid Mech.* **647** 221
[35] Sankararaman S and Ramaswamy S 2009 *Phys. Rev. Lett.* **102** 118107
[36] Joanny J F and Ramaswamy S 2012 *J. Fluid Mech.* **705** 46
[37] Khoromskaia D and Alexander G P 2015 *Phys. Rev.* E **92** 062311
[38] Chaikin P M and Lubensky T C 1995 *Principles of Condensed Matter Physics* (Cambridge: Cambridge University Press)
[39] Lubensky T C and Prost J 1992 *J. Phys.* II **2** 371
[40] Denniston C 1996 *Phys. Rev.* B **54** 6272–5
[41] Pismen L M 2013 *Phys. Rev.* E **88** 050502
[42] Vitelli V and Nelson D R 2006 *Phys. Rev.* E **74** 021711
[43] Kruse K, Joanny J F, Jülicher F, Prost J and Sekimoto K 2004 *Phys. Rev. Lett.* **92** 078101
[44] Nelson D R 2002 *Nano Lett.* **2** 1125–9
[45] Nedelec F J, Surrey T, Maggs A C and Leibler S 1997 *Nature* **389** 305
[46] Selinger R L B, Konya A, Travesset A and Selinger J V 2011 *J .Phys. Chem.* B **115** 13989–93
[47] De Gennes P-G 1976 *Mol. Cryst. Liq. Cryst.* **34** 177–82
[48] Zhang R, Zhou Y, Rahimi M and de Pablo J J 2016 *Nat. Commun.* **7** 1–9
[49] Pairam E, Vallamkondu J, Koning V, van Zuiden B C, Ellis P W, Bates M A, Vitelli V and Fernandez-Nieves A 2013 *Proc. Natl Acad. Sci. USA* **110** 9295